

# A NEW APPROACH TO AUTOMATIC SEGMENTATION OF SEMT IMAGES, BASED ON LOCAL EXTREMA

by

Martin Salzer<sup>1</sup>, Simon Thiele<sup>2</sup>, Roland Zengerle<sup>2</sup> and  
Volker Schmidt<sup>1</sup>

<sup>1</sup>Institute for Stochastics, Faculty of Mathematics, Ulm University, D-89069 Ulm, Germany

<sup>2</sup>Laboratory for MEMS Applications, IMTEK – Department of Microsystems Engineering, University of Freiburg, D-79110 Freiburg, Germany

E-mail: martin.salzer@uni-ulm.de, simon.thiele@imtek.uni-freiburg.de, zengerle@imtek.uni-freiburg.de, volker.schmidt@uni-ulm.de

Abbreviated running title: On segmentation of SEMt images

Abbreviated authors: Salzer M *et al.*

Key words: 3D Imaging, FIB-SEM Tomography, Porous Media, Segmentation

## ABSTRACT

A new algorithmic approach to segmentation of highly porous 3D image data gained by FIB-SEM tomography (SEMt) is described. The SEMt technique has shown to be useful in more and more fields of research, in particular for the development of new functional materials. However, algorithmic segmentation of SEMt images is a challenging problem for highly porous materials if filling the pore phase, e.g. with epoxy resin, is difficult. The grey intensities of individual voxels are not sufficient to determine the phase represented by them and usual thresholding methods are not applicable. We thus propose a new approach to segmentation of SEMt images. It consists in detecting the first and last occurrences of individual substructures by analysing the variation of grey intensities in  $z$ -direction. As an application, the segmentation of SEMt images for a cathode material used in polymer electrolyte membrane fuel cells is discussed.

## INTRODUCTION

In the next decades humanity has to face the problem of global climate change which is linked to our societies present and future energy consumption. Replacing fossil fuels and internal combustion engines by hydrogen and fuel cells is regarded as a key solution for future sustainable energy supply (Dunn, 2002). In particular, polymer electrolyte membrane fuel cells (PEMFC) are important energy converters delivering electric energy from chemical energy. In the PEMFC reaction, hydrogen and oxygen are converted to water. For a controlled performance of this reaction a high level of technological know-how especially in the membrane electrode assembly (MEA) is mandatory (Shao *et al.*, 2008). This approximately 40  $\mu\text{m}$  thick structure consists of an anode catalyst layer, a polymer electrolyte membrane (PEM) and a cathode catalyst layer (CCL). In the anode catalyst layer hydrogen molecules are catalytically split into electrons and protons. The PEM conducts protons to the anode but does not conduct electrons. The electrons can be conducted to the CCL via an electric circuit thereby providing electric energy. Finally, in the CCL, the protons, electrons and oxygen have to be transported to platinum catalyst sites where the crucial oxygen reduction reaction takes place.

There is no doubt that the 3D CCL morphology has a large impact on the performance of PEMFCs (Mezedur *et al.*, 2002). To better understand the influence of CCL morphology on rate limiting processes, several approaches have been developed to create artificial CCL morphologies (Siddique and Liu, 2010). However, since the CCL morphology is considerably influencing the transport processes within PEMFC, methods are required for the correct reconstruction of real CCL morphologies in 3D. The method which is currently best suited for this purpose is Focused Ion Beam (FIB) / Scanning Electron Microscope (SEM) tomography (shortly called SEMt in this paper). Note that SEMt is an advanced imaging technique which has successfully been used in materials science, e.g. for ceramics (Holzer *et al.*, 2004; Gaiselmann *et al.*, 2013), batteries (Hutzenlaub *et al.*, 2012; Stenzel *et al.*, 2013) and PEMFC cathodes (Ziegler *et al.*, 2011; Thiele *et al.*, 2011). But algorithmic segmentation of SEMt images is a challenging problem for highly

porous materials especially if it is difficult to fill the pore phase, e.g. with epoxy resin. In this case the grey intensities of individual voxels are not sufficient to determine the phase represented by them and usual thresholding methods are not applicable. We thus propose a different approach to segmentation of SEMt images, which is an extension of an algorithm recently introduced in (Salzer *et al.*, 2012) for the segmentation of SEMt images of another type of porous material.

In the present paper, our algorithm is applied to SEMt images for CCL material, where we detect the first and last occurrences of individual substructures by analysing the variation of grey intensities in  $z$ -direction. The algorithm is validated by comparing its segmentation results with those obtained by thresholding methods and by a manual segmentation approach (Thiele *et al.*, 2011), which is both subjective and time consuming.

The paper is organized as follows. We first describe the material and image data that is used as an example of application of our approach. Then, we introduce our method of automatic image segmentation. Subsequently, we discuss the obtained segmentation results and compare them to those which have been received by global thresholding and manual segmentation, respectively. A final section concludes and gives an outlook to possible future research.

## PRELIMINARIES

### DESCRIPTION OF MATERIAL AND IMAGING TECHNIQUE

In this study, a pristine commercial Gore PRIMEA A510.1 M710.18 C510.4 PEMFC membrane electrode assembly was used to carry out all tomographic experiments, see Fig. 1a. For this material, water modeling and imaging techniques complementary to SEMt have been studied e.g. in (Hutzenlaub *et al.*, 2012; Thiele *et al.*, 2013) but without establishing any automatic image segmentation.

← insert Fig. 1

The loading which is mass of Pt per surface area was  $0.1 \text{ mg/cm}^2$  at the anode and  $0.4 \text{ mg/cm}^2$  at the cathode. The CCL has a thickness of about  $11 \text{ }\mu\text{m}$  while the thickness of the anode catalyst layer is about  $3.5 \text{ }\mu\text{m}$ .

For SEMt a FIB for cutting and an SEM for the imaging are positioned in an angle of  $50^\circ$ – $54^\circ$ . With the FIB, gallium ions are accelerated towards the surface of the investigated sample provoking a very local sputtering process with spot sizes of  $10 \text{ nm}$  and less. The FIB thereby enables to remove slices from the sample, see Fig. 1b. Successive slicing by FIB and image acquisition by SEM produces a stack of 2D images.

## PREPROCESSING

Due to the different angles of the FIB and the SEM the obtained images contain a significant drift in  $y$ -direction that increases in  $z$ -direction. Correcting this drift is essential, as the algorithm described below strongly relies on correct alignment.

To accomplish this, we used a modified version of the least-square difference algorithm described in (Sarjakoski and Lammi, 1996). The algorithm determines the vector that leads to the smallest difference between two images when they are shifted in the direction of the vector. We modify this approach by only accounting voxels below a certain threshold ( $\tau_{\text{shift}} = 75$ ). This guarantees that the alignment is computed based on the background structures we try to detect later on. Additionally, we use linear interpolation to estimate grey intensities for values of non-integral coordinates. The drift is then determined by computing the difference between slice  $z$  and its successor  $z + 1$  for all shift vectors  $(s_x, s_y) \in \{-10, -9.5, -9, \dots, 9.5, 10\}^2$  where we determine the shift vector that leads to the minimal difference. Finally, we apply a 2D mean value filter with radius  $r = 1.0$  to the image.

## BASIC NOTATION

We denote by  $I$  the preprocessed image obtained by SEMt as described above, where  $I$  is a function that maps each voxel location  $(x, y, z)$  to its corresponding grey intensity

$I(x, y, z)$ , also denoted by  $I_{xy}(z)$  in the following.

## IMAGE SEGMENTATION

In this section we present a new approach to segmentation of SEMt images. This approach extends the key-principle of local threshold backpropagation described in (Salzer *et al.*, 2012). There, we detected sudden drops in grey intensity for given  $x$  and  $y$  coordinates and stepwise increasing  $z$ -values. We then used the last grey intensity before the drop to estimate a reasonable threshold that was used to detect the beginning of the currently visible structure. This idea, however, was based on the assumption that grey intensities remain the same within each substructure (while different substructures may have different grey values). However, this assumption does not hold for all datasets in particular not for the currently analyzed one: For many substructures we find a huge variation of the grey intensity. This is caused by various properties of the material that have an impact on the grey intensity. For example rough surfaces lead to higher grey intensities than surfaces with similar properties that are smoothed by the sputtering effect of the FIB. Additionally, some of the electrons that enter the specimen vanish in the material instead of being reflected by it. These electrons can not be detected by the sensor which leads to a lower grey value intensity. The sum of these influenceal properties result in a dataset where neither global nor common local thresholding schemes lead to sufficiently good results. Even more advanced techniques like the approach presented in (Salzer *et al.*, 2012) are not able to cover the complexity of the given data. Therefore we developed a new approach the basic idea of which is given below.

← insert Fig. 2

## SEGMENTATION PRINCIPLE

For any given pair  $(x, y)$  we consider the 1D restriction  $I_{xy}$  of the image  $I$ . Within this image we detect both phase shifts, i.e. the first and the last occurrence of a substructure, by looking for local maxima and minima, respectively. This is based on the following heuristic principle: When a substructure is visible but still located in the background its

grey intensity at this point is still relatively low. With each layer the FIB cuts off the structure gets closer to the sensor and the corresponding grey intensity increases. This continues until the substructure reaches the active slice. Therefore, we assume the grey intensity to reach a local maximum at the substructure's first occurrence, see Fig. 2. For the last occurrence of a substructure an analogous assumption is made. When a structure is being cut off by the FIB the pore space behind becomes visible. Due to the greater distance of the following substructure that is separated by the just recently revealed pore space, the corresponding grey intensity is supposed to be significantly lower. Thus, we assume to reach a local minimum after the last occurrence of a substructure.

## DETECTING LOCAL EXTREMA

We attempt to detect local minima and maxima within a 1D image  $I_{xy}$ , which we assume to be the last and first occurrence of a substructure, respectively. Due to the above described variations in grey intensity, we need to distinguish local extrema that represent the first or last occurrence of substructures from those that are based on variations on grey intensities within substructures. Therefore we introduce the following definitions for local extrema. We define that  $I_{xy}(z)$  represents a *local minimum* if both of the following two criteria are met: 1)  $I_{xy}(z) < I_{xy}(z + \Delta)$  for each  $\Delta \in \{-1, 1\}$ , and 2)  $I_{xy}(z') - I_{xy}(z) > \tau_{\min}$ , where  $z'$  denotes the location of the last *weak* maximum defined by

$$z' = \max\{z' < z : I_{xy}(z') > \max\{I_{xy}(z' - 1), I_{xy}(z' + 1)\}\}.$$

Furthermore, we say that  $I_{xy}(z)$  represents a *local maximum* if both of the following two criteria are met: 1)  $I_{xy}(z) > I_{xy}(z + \Delta)$  for each  $\Delta \in \{-1, 1, 2\}$ , and 2)  $I_{xy}(z) - I_{xy}(z^*) > \tau_{\max}$ , where  $z^*$  now denotes the location of the last minimum as defined above.

Note that these definitions are not fully symmetric, but there are two major differences. First, the grey intensity at voxel  $z$  is not only tested against the intensity at  $z \pm 1$  but also against  $z + 2$ . This is to compensate for the fact that the speed the grey intensity increases is significantly slower than the decrease we try to detect. Therefore, smaller

measurement errors, e.g. induced by false alignment, can lead to premature local maxima. Testing it against one additional grey intensity prevents the detection of some of these artificial local maxima. The difference in the characterization of local minima and local maxima is also the reason why we use two different thresholds ( $\tau_{\min}$  and  $\tau_{\max}$ ) to check for significance. When detecting local minima it is useful to use a higher value for  $\tau_{\min}$  to prevent within-structural variations from being classified as last occurrences. Local maxima, on the other hand, are ignored when they appear within a structure and therefore lower values for  $\tau_{\max}$  can be used.

Second, the grey intensity of a local minimum is not compared to the last local maximum but instead to the last *weak* local maximum. As the grey intensity of a substructure may change during time its grey intensity at the first occurrence is not a reasonable point of reference. The last *weak* maximum is closer to the currently tested local minimum and therefore more likely to provide a reasonable grey intensity.

## DESCRIPTION OF THE ALGORITHM

We now employ the concepts stated above to give a complete description of the algorithm. For every pair  $(x,y)$  perform the following steps:

1. Denote the first local minimum by  $b_{xy}^0$ .
2. Set  $k$  to 1.
3. Compute  $a_{xy}^k = \min\{z > b_{xy}^{k-1} : z \text{ local maximum}\}$ .
4. Compute  $b_{xy}^k = \min\{z > a_{xy}^k : z \text{ local minimum}\}$ . If no local minima are left set  $b_{xy}^k$  to  $z_{\max} + 1$  where  $z_{\max}$  denotes the highest possible  $z$  value.
5. If there are local maxima left, increase  $k$  by 1 and continue with step 3.

Every interval  $[a_{xy}^k, b_{xy}^k - 1]$  now represents the estimated life span of a substructure

and the resulting binary image is given by

$$B_{\text{extrema}}(x, y, z) = \begin{cases} 255, & \text{if } z \in \bigcup_{k=1}^{k_{xy}^{\max}} [a_{xy}^k, b_{xy}^k - 1], \\ 0, & \text{otherwise.} \end{cases}$$

## POSTPROCESSING

Due to the complex nature of SEMt images the approach described above is not able to classify every voxel correctly. However, most of the occurring problems can be removed by appropriate postprocessing. First, we set  $B_{\text{extrema}}^*(x, y, z) = 0$  if  $I(x, y, z) < \tau$ , where  $\tau$  is a manually chosen threshold. Then we remove small isolated clusters of foreground voxels by applying two 2D range filters (in our case with  $r_1 = 2, \alpha_1 = 0.5$  and  $r_2 = 10, \alpha_2 = 0.15$ ). Finally, we perform a dilation with radius  $r_{\text{dil}} = 4.5$ , which is limited to voxel with a grey intensity in the original image  $I$  above the previously chosen threshold  $\tau$ . This dilation connects otherwise separated voxel to a large set of connected regions and provides the final outcome of our approach. Figure 3 provides an illustration for all postprocessing steps.

In the first two steps, the parameter  $\tau$  and the corresponding radii  $r_{1/2}$  and quantiles  $\alpha_{1/2}$  for the range filters are chosen to provide a good optical fit. The parameter  $r_{\text{dil}}$  for the dilation, which is the most influential step, is chosen to match the original volume fraction of the material, which is a commonly known property of most specimen.

← insert Fig. 3

## RESULTS

We now present the segmentation results, which have been obtained by our algorithm, and compare them to those of a global thresholding and a manual segmentation. The manual segmentation was performed by first applying a certain global threshold and then manually correcting the images using the software gimp (Thiele *et al.*, 2011). Furthermore, a local thresholding approach has been tested. However the best results were

obtained for a window size equal to the dimension of the image, i.e., it turned out that the best local thresholding is identical with global thresholding.

← insert Fig. 4

## VISUAL COMPARISON OF SEGMENTED IMAGES

A visual comparison of 2D slices (see Figure 4) indicates a significant improvement which has been achieved by the automatic segmentation algorithm proposed in the previous section. This is also reflected by the rate of erroneously classified voxels, which was reduced to 16.7% (thresholding 22.5%), supposing that the manual segmentation is correct. Both phases are now being detected by a probability above 80%, with background voxel being detected more often (85.7%) than foreground voxels (80.7%). Visual inspection shows that some of the missing foreground voxels are false positives in the manual segmentation, which is, due to the huge time consumption, always limited in detail. For more information, see Table 1, where the rates for correct and wrong classification of foreground and background voxels, respectively, are given, comparing the results of manual segmentation with those of automatic segmentation as proposed in the previous section. In brackets the corresponding rates are given for the comparison of manual segmentation and global thresholding.

Although the rates given in Table 1 show a clear advantage of the segmentation approach proposed in this paper relative to global thresholding, they do not fully capture the improvement which has been achieved with respect to correct reconstruction of the 3D morphology. This will be discussed in the following section.

← insert Table 1

## SPHERICAL CONTACT DISTRIBUTION FUNCTION

The spherical contact distribution function (SCDF) is a common tool in stochastic geometry to compare the 3D morphologies of random sets (Stoyan *et al.*, 1995). For binary image data, the empirical SCDF is given by the cumulative distribution function of the distances of all background (foreground) voxel to their nearest foreground (background) voxel, respectively. Fig. 5 shows the empirical SCDF of both background and foreground

for the three segmentation approaches considered in this paper. In both cases the result provided by the automatic segmentation algorithm proposed in this paper is significantly closer to the empirical SCDF of the manual segmentation than that corresponding to thresholding. ← *insert Fig. 5*

Furthermore, two difference images have been analysed which were constructed by voxel-wise comparison of the manually segmented image with the automatically segmented image and the image obtained by global thresholding, respectively. The empirical SCDF of these two difference images are visualized in Fig. 6. They show that in the automatically segmented image more than half of the misclassified voxels have a correctly classified neighbour and, therefore, are presumed not to have a larger impact on the morphological properties of the image. The main difference between the binarisation obtained by the new approach proposed in this paper and global thresholding occurs for greater radii between 2 and 6. This suggests that the new approach preserves significantly more features of the original 3D morphology. ← *insert Fig. 6*

## SUMMARY AND DISCUSSION

We have proposed a new approach to automatic segmentation of SEMt images. This approach was developed by following the key-principle of analysing the variation of grey intensities in  $z$ -direction which has recently been developed in (Salzer *et al.*, 2012). Therefore, we introduced the notions of error-tolerant local maxima and minima and introduced threshold criteria to distinguish them from (smaller) extrema with substructures. These local maxima and minima then are used as an indicator for the beginning and end of substructures, respectively. From this preliminary segmentation we derived a final binarisation by some postprocessing which consists of a thresholding, cluster-detection and dilation. The final result was then analysed and compared with those obtained by manual segmentation and global thresholding. It turned out that the segmented image, which has been obtained by the new approach considered in this paper, preserves significantly more

features of the original 3D morphology than this is possible by global thresholding.

## REFERENCES

- Dunn S (2002). Hydrogen futures: toward a sustainable energy system. *International Journal of Hydrogen Energy* 27:235–64.
- Gaiselmann G, Neumann M, Holzer L, Hocker T, Prestat MR, Schmidt V (2013). Stochastic 3D modeling of  $\text{La}_{0.6}\text{Sr}_{0.4}\text{CoO}_{3-\delta}$  cathodes based on structural segmentation of FIB-SEM images. *Computational Materials Science* 67:48–62.
- Holzer L, Indutnyi F, Gasser P, Munch B, Wegmann M (2004). Three-dimensional analysis of porous  $\text{BaTiO}_3$  ceramics using FIB nanotomography. *Journal of Microscopy* 216:84–95.
- Hutzenlaub T, Thiele S, Zengerle R, Ziegler C (2012). Three-dimensional reconstruction of a  $\text{LiCoO}_2$  Li-ion battery cathode. *Electrochemical and Solid State Letters* 15:A33–A36.
- Mezedur M, Kaviany M, Moore W (2002). Effect of pore structure, randomness and size on effective mass diffusivity. *AIChE Journal* 48:15–24.
- Salzer M, Spetl A, Stenzel O, Smått JH, Lindén M, Manke I, Schmidt V (2012). A two-stage approach to the segmentation of fib-sem images of highly porous materials. *Materials Characterization* 69:115–26.
- Sarjakoski T, Lammi J (1996). Least square matching by search. *Proceedings of the XVIII ISPRS Congress Vienna Austria XXXI:724–8*.
- Shao Y, Liu J, Wang Y, Lin Y (2008). Novel catalyst support materials for pem fuel cells: current status and future prospects. *Journal of Materials Chemistry* 19:46–59.
- Siddique N, Liu F (2010). Process based reconstruction and simulation of a three-dimensional fuel cell catalyst layer. *Electrochimica Acta* 55:5357–66.
- Stenzel O, Westhoff D, Manke I, Kasper M, Kroese D, Schmidt V (2013). Graph-based simulated annealing: A hybrid approach to stochastic modeling of complex

microstructures. *Modelling and Simulation in Materials Science and Engineering* in print.

Stoyan D, Kendall WS, Mecke J (1995). *Stochastic geometry and its applications*. Chichester: J. Wiley & Sons.

Thiele S, Fürstenhaupt T, Banham D, Hutzenlaub T, Birss V, Ziegler C, Zengerle R (2013). Multiscale tomography of nanoporous carbon-supported noble metal catalyst layers. *Journal of Power Sources* 228:185–92.

Thiele S, Zengerle R, Ziegler C (2011). Nano-morphology of a polymer electrolyte fuel cell catalyst layer—imaging, reconstruction and analysis. *Nano Research* 4:849–60.

Ziegler C, Thiele S, Zengerle R (2011). Direct three-dimensional reconstruction of a nanoporous catalyst layer for a polymer electrolyte fuel cell. *Journal of Power Sources* 196:2094–7.

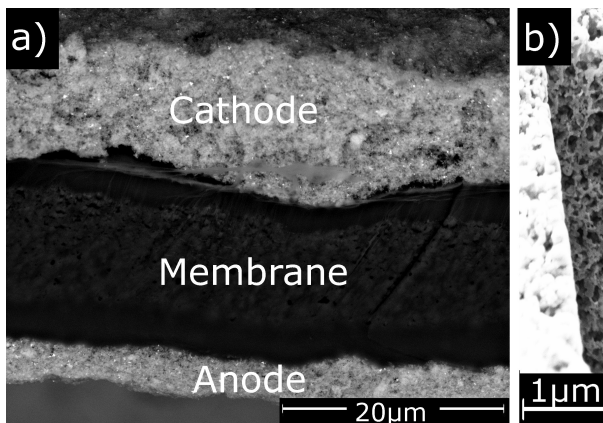


Fig. 1: Membrane electrode assembly with cathode, anode and membrane (a); cavity in the cathode opened by FIB (b)

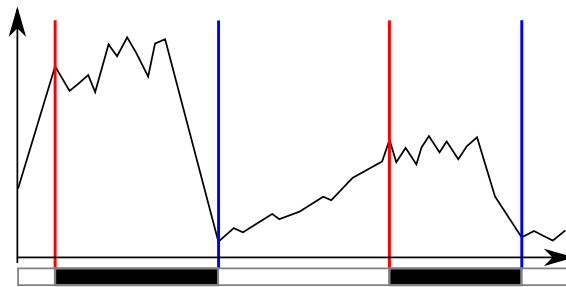


Fig. 2: Schematic 1D example for the detection of local maxima (red) and minima (blue). The bar below shows the binarised image

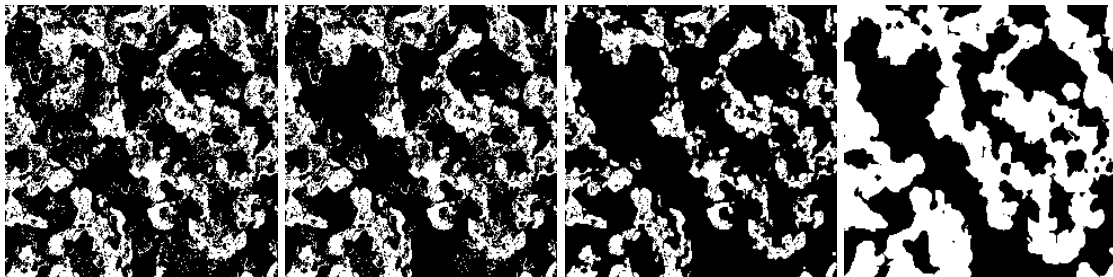


Fig. 3: *From left to right: before postprocessing; after thresholding; isolated clusters removed; dilation and final result*

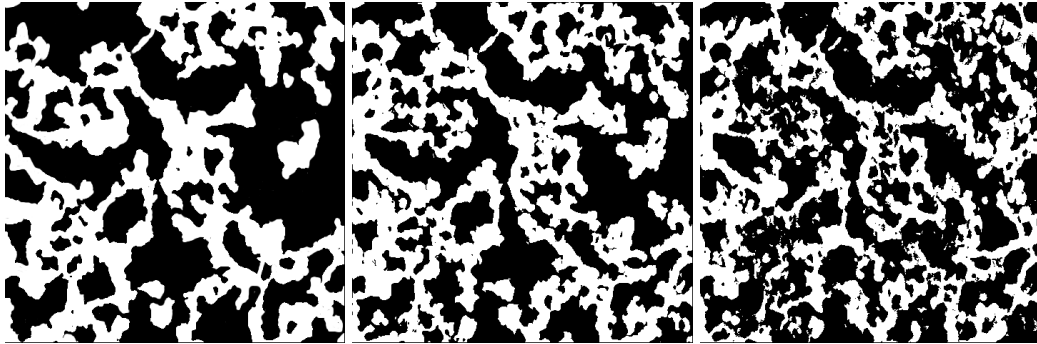


Fig. 4: *From left to right: manual segmentation; automatic segmentation as stated in this paper; global thresholding*

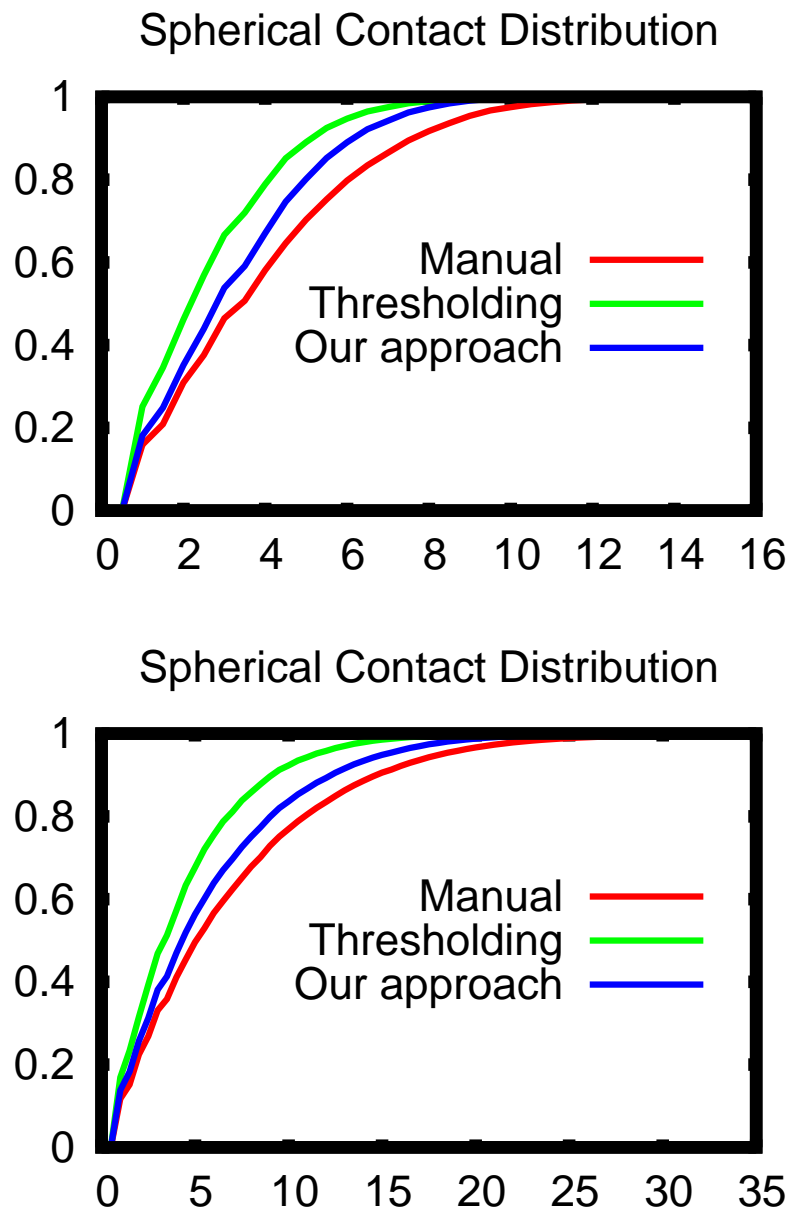


Fig. 5: Empirical SCDF for foreground (top) and background (bottom)

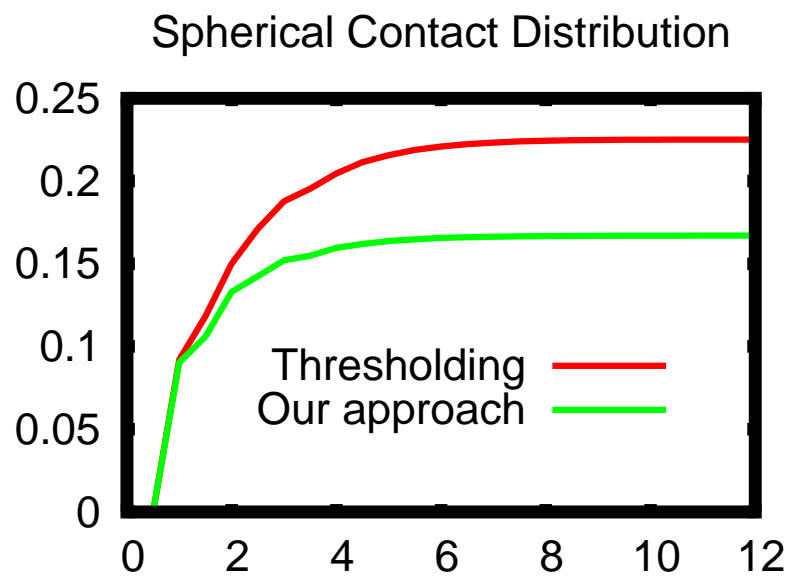


Fig. 6: Empirical SCDF for difference images describing sets of misclassified voxels

classified as	FG manually	BG manually
FG automatic (FG thresholding)	80.7% (71.5%)	14.3% (18.2%)
BG automatic (BG thresholding)	19.3% (28.5%)	85.7% (81.8%)

Table 1: *Detection rates for foreground (FG) and background (BG) voxels*